SUPPLEMENTAL MATERIAL

Search for Gamma-ray Spectral Lines from Dark Matter Annihilation up to 100 TeV towards the Galactic Center with MAGIC (The MAGIC Collaboration)

Model choices and parameters for the Milky Way dark matter density distribution

In this work, we have described the Milky Way (MW) dark matter (DM) halo with analytic prescriptions commonly adopted in the literature, with parameters fit either to simulation results or kinematic data. For the different models, we have made use of the Einasto profile [1]:

$$\rho_{\rm Einasto}(r) = \rho_s \exp\left\{ \frac{-2}{\alpha}\left[\left(\frac{r}{r_s}\right)^{\alpha} - 1\right]\right\}, \tag{1}$$

the Hernquist-Zhao (α, β, γ) profile [2, 3]:

$$\rho_{\rm Zhao}(r) = \frac{2^{\frac{\beta-\gamma}{\alpha}}\rho_s}{\left(\frac{r}{r_s}\right)^{\gamma}\left[1+\left(\frac{r}{r_s}\right)^{\alpha}\right]^{\frac{\beta-\gamma}{\alpha}}}, \tag{2}$$

as well as the cored Burkert model [4]:

$$\rho_{\rm Burkert}(r) = \frac{\rho_s}{\left(1+\frac{r}{r_s}\right)\left(1+\frac{r^2}{r_s^2}\right)}. \tag{3}$$

For the two considered cases describing a steep DM density cusp in the inner Galactic halo, we have adopted the Einasto profile with $\alpha = 0.17$ and Navarro-Frenk-White (NFW, Eq. (2) with $\alpha = 1$, $\beta = 3$, $\gamma = 1$) descriptions from [5], but with slightly modified values of ρ_s as used in [6, 7], calibrating the local DM density $\rho_\odot$ (and consequently, the halo mass) to a marginally lower value. Although recent analyses using data from the GRAVITY experiment and GAIA satellite suggest a somewhat higher value in the range of $0.4 - 0.8\,{\rm GeV\,cm^{-3}}$ [8, 9], the chosen values are still in the allowed observational range, and we have kept the profiles identical to [6, 7] to ease comparison of the results.

While standard ΛCDM cosmology predicts scale-invariant cuspy density profiles of DM halos [10], the presence of baryons can significantly alter the inner cusps of DM halos. The impact of baryonic physics onto the DM profile is complex with counter-acting processes: the DM density is expected to flatten by non-adiabatic feedback by star formation and supernova winds [11], while in turn baryonic energy and angular momentum dissipation contract the DM profile [12]. Different processes dominate on different galaxy mass scales, with no clear trend for the behavior of a MW-sized galaxy [13–15]. While cores not larger than $0.5 - 1\,{\rm kpc}$ in radius are generally expected to form in MW-like galaxies [16–18], a core as large as several kpc in radius is not excluded observationally for the MW, and is preferred in fits with a fixed flat DM distribution at the Galactic Center (GC) as the Burkert profile from [19] and Hernquist-Zhao profile with $\alpha = 1$, $\beta = 3$, $\gamma = 0$ from [20] investigated in this paper. We remark that even the less conservative case [20] of our two considered core models provides a DM density in the inner GC region a factor 3 smaller than an Einasto halo with a flat core within 1 kpc in radius, and even a factor 10 smaller densities compared to such Einasto profile cored at 0.5 kpc (see Fig. 1, left).

In Tab. I, we list the choices of parameters adopted for the different density profile models. We provide the density normalization both in terms of the profile scale radius, $\rho_s = \rho(r_s)$, as well as the local DM density at the Solar circle, $\rho_\odot = \rho(R_\odot)$. $R_{\rm max}$ denotes, as a measure of the MW virial radius, the maximum radius at which we stopped the line-of-sight integration according to Eq. (3) of the main paper.

In Tab. II, we provide the J-factor values integrated according to Eq. (3) of the main paper within a radius corresponding to the one of the region of interests (ROIs, see Fig. 2) centered on the GC. In Fig. 1, we compare the different adopted density models (left) and resulting J-factors as a function of angular distance from the GC (right).

Profile name	Profile type	α	β	γ	ρ_s [GeV cm^{-3}]	r_s [kpc]	$\rho_\odot$ [GeV cm^{-3}]	$R_\odot$ [kpc]	$R_{\rm max}$ [kpc]	Reference
Cuspy Einasto	Einasto	0.17	–	–	0.0790	20	0.388	8.5	433	[5–7]
NFW	Zhao	1	3	1	0.0768	21	0.384	8.5	402	[5–7]
Cored Zhao	Zhao	1	3	0	0.431	7.7	0.391	8.21	265	[20]
Burkert core	Burkert	–	–	–	1.568	9.26	0.487	7.94	291	[19]

TABLE I. Parameter choices and selected halo properties of the Galactic DM density models considered in this work. Note the different definition of ρ_s in the Hernquist-Zhao profile of Eq. (2). when comparing against [6, 7, 20]. For the Einasto and NFW profiles, $R_{\rm max}$ is taken from [5]. For the Hernquist-Zhao and Burkert core profiles, we chose $R_{\rm max}$ such that to obtain the halo masses given in [19] and [20].

Profile name	$J(0.5^\circ)$	$J(1.0^\circ)$	$J(1.1^\circ)$
Cuspy Einasto	3.14×10^{21}	8.01×10^{21}	9.03×10^{21}
NFW	2.18×10^{21}	4.55×10^{21}	5.02×10^{21}
Cored Zhao	2.66×10^{19}	1.06×10^{20}	1.28×10^{20}
Burkert core	1.26×10^{19}	5.04×10^{19}	6.10×10^{19}

TABLE II. J values integrated within a radius corresponding to the one of the ROIs, i.e. 0.5°, 1.0°, and 1.1°, around the direction towards the GC (see Fig. 2) and models from Tab. I. All values are given in units of GeV^2 cm^{-5}.

Observational dataset and definition of the region of interest

The GC has been observed over many years by MAGIC. During these years, several upgrades of the instrument have been deployed and different pointing directions were used. Therefore, our dataset is divided into nine subsets of constant instrumental conditions and pointing offsets, listed in Tab. III. For all subsets, data was taken with the telescopes pointing slightly offset from the GC (SgrA*), with different offsets and different directions. Fig. 2 illustrates the various pointing directions in Galactic coordinates around the GC. Our ROIs are circular regions of 0.5°, 1.0°, and 1.1° in radius around the GC position, depending of the telescopes' pointing direction in the data subsets, and are marked by the respective circles. Note that by this configuration, the ROIs are located at different positions in the telescopes' field of view, depending on the pointing. By these ROI choices, the maximum distance of a reconstructed event from the camera center used in the analysis is kept below 1.5° for all data subsets.

The total observation time reached about 260 hours. We applied various selection cuts to ensure the data quality. Main selection cuts were based on (1) the atmospheric transmission, (2) the night-sky background, and (3) the shower image quality. For (1), a LIDAR was measuring the differential transmission of the atmosphere during the observations. We removed from the dataset time periods with less than 80 % atmospheric transparency. For (2), the direct current of the photomultiplier tubes in the camera reflects the sky brightness, also an indicator of the weather conditions:

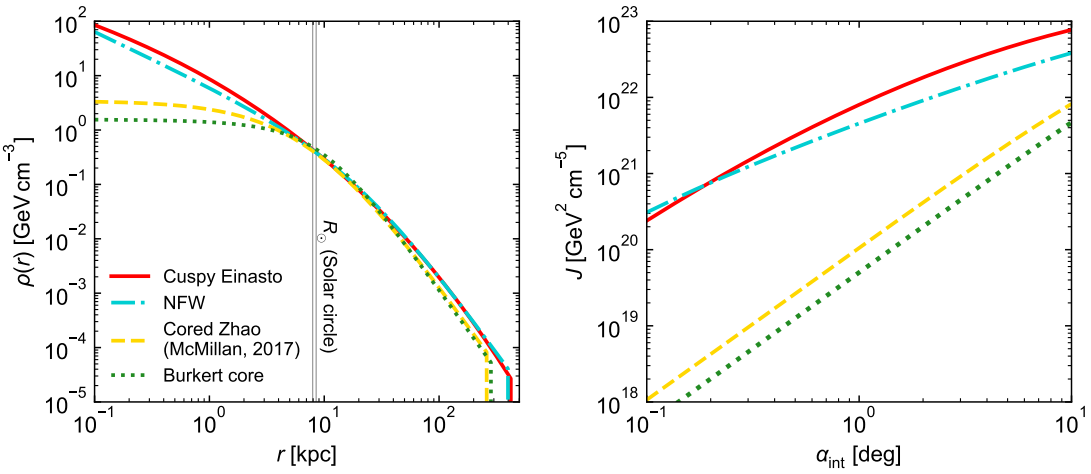

FIG. 1. Comparison of the different density models and resulting J-factors for the spherical MW DM halo considered in this work. Left: spherical density profiles. Right: corresponding J-factors within circular integration regions centered at the GC and radius $\alpha_{\rm int}$.

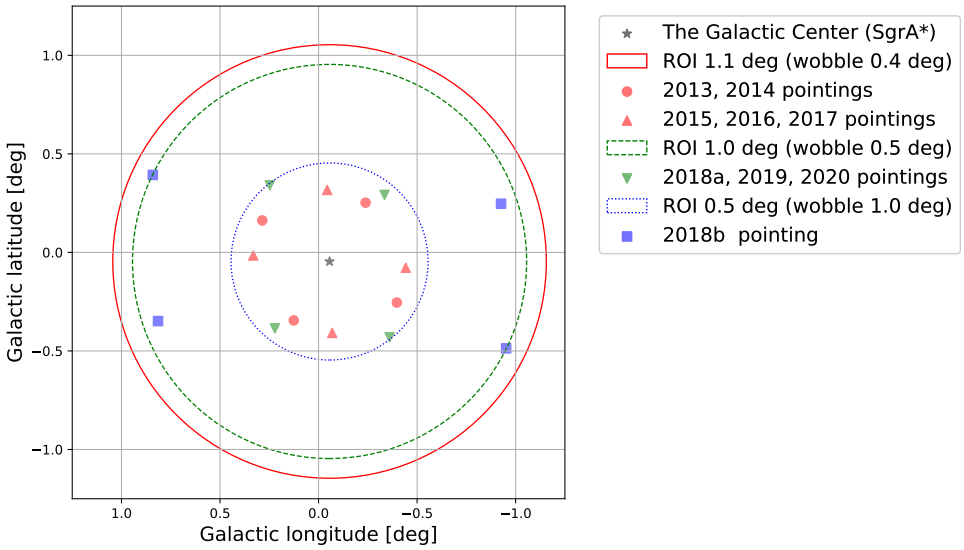

FIG. 2. Pointing positions (Galactic coordinates) of the MAGIC telescopes in the used data subsets and adopted ROIs. The markers show the pointing directions. The position of the GC is displayed with a black star, around which the ROIs of our analysis are centered for all data subsets. The ROI encircled by the red solid line has a radius of 1.1° and is used for the data from 2013 and 2014 with the telescope pointings marked by the red dots, and for and 2015 and 2016 with the pointings marked by red upright triangles. The ROI indicated by the green dashed circle has a radius of 1.0° and is used for the data from 2018 to 2019 using the pointings marked by the green upside down triangles. The blue dotted solid circle shows the ROI with 0.5° radius for the data taken in 2018 with the pointings marked by the blue squares.

when clouds appear in the sky, they reflect light from the ground and the sky brightness increases. The typical value for a direct current cut is requiring less than 1.4 μA for MAGIC-I and 3.0 μA for MAGIC-II during astronomical dark time. For (3), a cut on the minimal total charge contained in a shower image is applied. We removed events that have less than 50 photoelectrons after the image cleaning procedure to efficiently suppress misreconstruction of the total charge by night sky background pollution. The night sky background rate is typically 100 - 120 MHz/pixel which corresponds to about ~ 0.17 photoelectron/pixel/ns.

Dates	Label	Total observation time [h] (before quality cuts)	Effective live time [h] (after quality cuts)
2013/03/10 – 2013/07/18	2013	47.1	38.8
2014/03/01 – 2014/07/07	2014	37.3	30.1
2015/03/29 – 2016/04/13	2015	27.0	18.9
2016/05/02 – 2016/08/05	2016	24.8	17.3
2017/03/26 – 2017/06/24	2017	26.0	22.1
2018/02/19 – 2018/09/30	2018a	26.3	19.1
	2018b	7.0	5.8
2019/03/11 – 2019/08/04	2019	54.4	52.0
2020/06/19 – 2020/08/21	2020	22.9	19.1
Total		272.8	223.2

TABLE III. Observational periods of constant instrumental conditions (specified by the time ranges) and pointing directio ns (see Fig. 2 and the label column), with their corresponding raw observation times and effective (i.e. dead time corrected) live times after quality cuts.

Determination of the background normalisation parameter τ_{obs} and its variance

To determine the likelihood parameters τ_{obs} and σ_τ, we chose suitable test datasets far off the GC and free of any known γ-ray signals, but in the same range of zenith angles as the GC dataset. We performed on these test data the same analysis as for the GC data according to Eq. (4) of the main paper. The analysis was applied on 20 independent

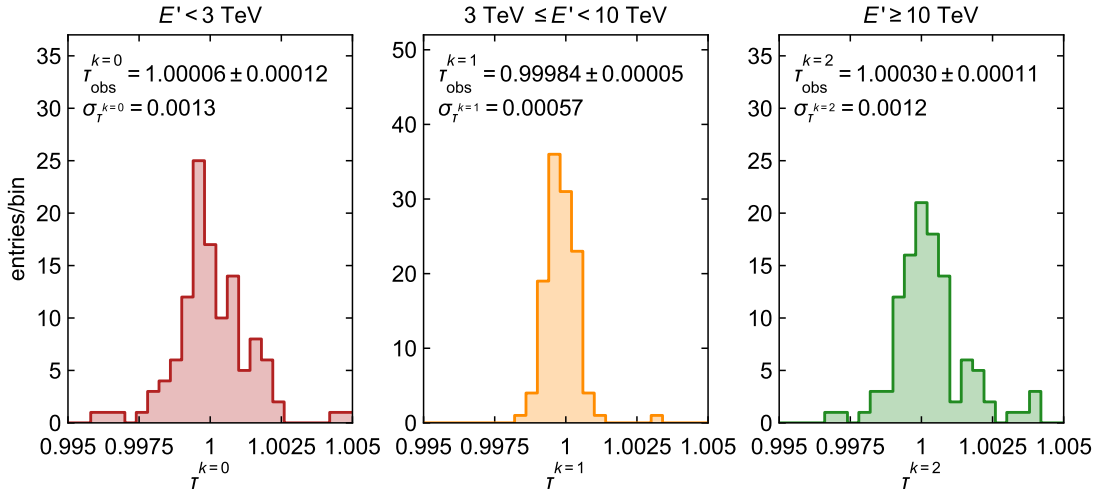

FIG. 3. Distributions of τ according to Eq. (4) when searching for line signals in the test data in the three energy intervals, based on 120 analyzed test datasets in each interval. It is found a small bias $\tau_{\rm obs} < 1$ for energies $E' \gtrsim 3$ TeV and $\sigma_{\tau^k} < 0.01\,\tau^k_{\rm obs}$. The statistical error according to Eq. (5) is $\sigma_{\tau^{k=0},\rm stat} = 2.60 \times 10^{-5}$, $\sigma_{\tau^{k=1},\rm stat} = 2.76 \times 10^{-5}$, and $\sigma_{\tau^{k=2},\rm stat} = 1.77 \times 10^{-4}$.

test datasets, all with a ROI radius of 1.1°, for each of the 18 probed DM masses, resulting in 360 samples in total. Then, for each of the samples, the quantity τ given by

$$\tau = \frac{N_{\rm ON} - N_{\rm sig}}{N_{\rm ON}} \tag{4}$$

was computed. The resulting distribution has the mean $\tau_{\rm obs}$ and statistical variance

$$\sigma^2_{\tau,\rm stat} = \left(\frac{\partial\tau}{\partial N_{\rm sig}} \times \sigma_{N_{\rm sig}}\right)^2 + \left(\frac{\partial\tau}{\partial N_{\rm ON}} \times \sigma_{N_{\rm ON}}\right)^2 , \tag{5}$$

where $N_{\rm ON}$ is the number of observed events in the sliding window, and $N_{\rm sig}$ the number of events associated to a fitted signal component. This procedure allowed us to consider a possible bias in $\tau_{\rm obs}$, i.e. $\tau_{\rm obs} \neq 1$. Furthermore, to take into account a potential energy dependence of $\tau_{\rm obs}$ and σ_τ, we calculated $\tau^k_{\rm obs}$ and σ_{τ^k} in three energy intervals ($k = 0, 1, 2$), namely, for $E' < 3\,$TeV, $3\,\text{TeV} \leq E' < 10\,$TeV, and $E' \geq 10\,$TeV, where in each interval we determined $\tau^k_{\rm obs}$ and of σ_{τ^k} from 120 samples by merging the analyses of six masses to increase the statistical power of the result. The observed total variance of τ in each energy interval can be written as

$$\sigma^2_{\tau^k} = \sigma^2_{\tau^k,\rm stat} + \sigma^2_{\tau^k,\rm syst}\,. \tag{6}$$

If σ_{τ^k} was only driven by the Poissonian fluctuations of the number of events, the variance would match the expected statistical uncertainty $\sigma_{\tau^k,\rm stat}$ according to Eq. (5). However, we found σ_{τ^k} to be dominated by $\sigma_{\tau^k,\rm syst}$, and obtained $\sigma_{\tau^k} \approx \sigma_{\tau^k,\rm syst} < 0.01\,\tau^k_{\rm obs}$ (see Fig. 3). It can be seen in Fig. 3 a small bias $\tau_{\rm obs} < 1$ for energies $E' \gtrsim 3$ TeV, attributed to the approximation of the background spectral shape by a power law in the sliding window. On the other hand, the width of σ_{τ^k}, taken into account in the likelihood fitting (see term (c) of Eq. (4) in the main paper), indicates a variation of the expected background spectral shape rendering this bias negligible.

[1] E. Retana-Montenegro, E. van Hese, G. Gentile, M. Baes, and F. Frutos-Alfaro, Astron. Astrophys. **540**, A70 (2012), arXiv:1202.5242 [astro-ph.CO].
[2] L. Hernquist, Astrophys. J. **356**, 359 (1990).
[3] H. Zhao, MNRAS **278**, 488 (1996), arXiv:astro-ph/9509122 [astro-ph].
[4] A. Burkert, Astrophysical Journal Letters **447**, L25 (1995), arXiv:astro-ph/9504041 [astro-ph].
[5] L. Pieri, J. Lavalle, G. Bertone, and E. Branchini, Phys. Rev. D **83**, 023518 (2011), arXiv:0908.0195 [astro-ph.HE].
[6] A. Abramowski *et al.* (H.E.S.S. Collaboration), Phys. Rev. Lett. **110**, 041301 (2013), arXiv:1301.1173 [astro-ph.HE].
[7] H. Abdallah *et al.* (H.E.S.S. Collaboration), Phys. Rev. Lett. **120**, 201101 (2018), arXiv:1805.05741 [astro-ph.HE].

[8] M. Benito, A. Cuoco, and F. Iocco, Journal of Cosmology and Astroparticle Physics **2019** (3), 033, arXiv:1901.02460 [astro-ph.GA].
[9] M. Benito, F. Iocco, and A. Cuoco, Physics of the Dark Universe **32**, 100826 (2021), arXiv:2009.13523 [astro-ph.GA].
[10] J. Wang, S. Bose, C. S. Frenk, L. Gao, A. Jenkins, V. Springel, and S. D. M. White, Nature (London) **585**, 39 (2020), arXiv:1911.09720 [astro-ph.CO].
[11] A. Pontzen and F. Governato, MNRAS **421**, 3464 (2012), arXiv:1106.0499 [astro-ph.CO].
[12] O. Y. Gnedin, A. V. Kravtsov, A. A. Klypin, and D. Nagai, Astrophys. J. **616**, 16 (2004), arXiv:astro-ph/0406247 [astro-ph].
[13] A. Di Cintio, C. B. Brook, A. V. Macciò, G. S. Stinson, A. Knebe, A. A. Dutton, and J. Wadsley, MNRAS **437**, 415 (2014), arXiv:1306.0898 [astro-ph.CO].
[14] E. Tollet, A. V. Macciò, A. A. Dutton, G. S. Stinson, L. Wang, C. Penzo, T. A. Gutcke, T. Buck, X. Kang, C. Brook, *et al.*, MNRAS **456**, 3542 (2016), arXiv:1507.03590 [astro-ph.GA].
[15] A. Lazar, J. S. Bullock, M. Boylan-Kolchin, T. K. Chan, P. F. Hopkins, A. S. Graus, A. Wetzel, K. El-Badry, C. Wheeler, M. C. Straight, *et al.*, MNRAS **497**, 2393 (2020), arXiv:2004.10817 [astro-ph.GA].
[16] F. Governato, A. Zolotov, A. Pontzen, C. Christensen, S. H. Oh, A. M. Brooks, T. Quinn, S. Shen, and J. Wadsley, MNRAS **422**, 1231 (2012), arXiv:1202.0554 [astro-ph.CO].
[17] A. Pontzen and F. Governato, Nature (London) **506**, 171 (2014), arXiv:1402.1764 [astro-ph.CO].
[18] V. Gammaldi, V. Avila-Reese, O. Valenzuela, and A. X. Gonzalez-Morales, Phys. Rev. D **94**, 121301 (2016), arXiv:1607.02012 [astro-ph.HE].
[19] F. Nesti and P. Salucci, Journal of Cosmology and Astroparticle Physics **2013** (7), 016, arXiv:1304.5127 [astro-ph.GA].
[20] P. J. McMillan, MNRAS **465**, 76 (2017), arXiv:1608.00971 [astro-ph.GA].